DAMAGE CONTROL AND OPTIMAL DESIGN OF EMBEDDED CFRP CIRCULAR TUBE CFSST COLUMN-H-BEAM JOINT WITH ENERGY-DISSIPATION ANGLE STEEL

Guo-Chang Li, Yong Ma *, Xiao Li, Wei-Qi Cui, Zhi-Bin Han and Zhuang-Wen Qin

School of Civil Engineering, Shenyang Jianzhu University, Shenyang 110168, China

* *(Corresponding author: E-mail: my052106@163.com)*

A B S T R A C T

Maintaining the integrity of the main structure during seismic events and enabling rapid restoration of its normal functionality afterwards are key design objectives in modern earthquake engineering. Based on the design concept of controllable damage and replaceable components after an earthquake, this study investigates a novel beam-column joint, consisting of an embedded carbon fiber-reinforced polymer (CFRP) circular tube concrete-filled square steel tube (CFSST) column and an H-beam equipped with energy-dissipation angle steel components (EDASCs). A numerical model was established using ABAQUS finite element software, and its accuracy was validated against typical experimental data. Joint models with varying material strengths of EDASCs, design bearing capacity coefficients, and free deformation lengths of spliced energy-dissipating beam sections (SEDBSs) were developed. The influence of various parameters on the seismic performance of beam-column joint and the functionality of "structural fuse" was investigated, leading to optimized design recommendations. The results show that during the plastic stage, the EDASCs accounted for 91% of the total energy dissipation of the joints, effectively protecting the main structure and achieving the design objectives of recoverability and replaceability. The material strength and thickness of the EDASCs significantly affect the seismic performance of the joint. In consideration of the bearing capacity, ductility, and energy dissipation ratio of the joint, Q235 steel is recommended as the material for the EDASCs. The design bearing capacity coefficient of the beam-column joint should range from 0.75-0.98 to achieve optimal seismic performance and fulfill the "structural fuse" function. The free deformation length of the SEDBSs should be set at 1-1.5 times the width of the beam flange.

A R T I C L E   H I S T O R Y

Received:	11 September 2025
Revised:	3 January 2026
Accepted:	4 January 2026

K E Y W O R D S

CFRP circular tube;
Concrete-filled square steel tube;
Energy-dissipation angle steel component;
Outer diaphragm;
Design bearing capacity coefficient

1. Introduction

Concrete-filled steel tube (CFST) members are widely used in super high-rise buildings and large-span spatial structures due to their excellent mechanical properties and economic benefits [1]. To address the issue of the relatively weak lateral confinement of concrete by square steel tubes in CFST members, Li G C [2-4] proposed a composite member of square steel tube with an embedded CFRP circular tube and systematically studied its mechanical properties under different working conditions. The research results show that the confinement effect of the CFRP circular tube on the core concrete can significantly enhance the bearing capacity of the square steel tube concrete composite member and improve its ductility. Currently, the research on square steel tube concrete members with embedded CFRP circular tubes is relatively mature, but the corresponding research on beam-column joints is still insufficient. To promote the application of this structural system, it is urgent to develop high-performance beam-column joints that match it.

As a critical load transfer component in CFST structures, the ductility, energy dissipation capacity, and post-earthquake repairability of beam-column joint are key factors determining the collapse resistance and lifecycle economy of the entire structure under rare earthquakes. In 2011, the seismic damage investigation following the M6.3 earthquake in Christchurch, New Zealand, revealed that numerous bolted-welded hybrid joints experienced brittle fractures in the flange weld areas due to the lack of a graded energy dissipation mechanism [5,6]. This phenomenon promoted the transformation in the seismic design concept of building structures from "collapse prevention design" to "recoverable design" [7-10], leading to the development of a two-stage elastic seismic design method based on performance. In the first stage, replaceable energy dissipation elements are employed to dissipate seismic energy, ensuring that the main structure remains in an elastic state; in the second stage, rapid structural function recovery is achieved by promptly replacing damaged components [11].

To enable rapid recovery of normal functionality for building structures after earthquakes, the development of recoverable and replaceable beam-column joints can be categorized into three stages. In the first stage, the application of various dampers to steel beam-column joints has demonstrated significant enhancement in both energy dissipation capacity and damage control ability within structural systems [12-14], laying a foundation for post-earthquake functional recovery. In the second stage, replaceable energy-dissipation components such as flange cover plates, web connecting plates, and angle steel components are employed, along with refined structural parameter controls [15-19]. This approach ensures that plastic damage is concentrated on the energy dissipation components, allowing post-earthquake repairs to focus solely on replacing these components. Studies indicate that replacing energy dissipation elements after quasi-static tests typically requires approximately 2 hours [20-24]. In the third stage, a fully bolted prefabricated connection system has been developed, utilizing a graded yield design strategy to ensure that the energy dissipation plate yields first. Both experimental results and finite element analyses confirm that the plastic damage of the joints is effectively concentrated on the energy dissipation plate while the main structure remains in an elastic state [25-30] .

Based on the above research, post-earthquake recoverable and replaceable beam-column joints primarily dissipate seismic energy through dampers, end plates, cover plates, connecting plates, and angle steels as "structural fuses" [9]. However, several key challenges remain: First, as the primary energy dissipation component, damper structures are complex, and dampers located outside the beam flange conflict with the enclosure systems, severely limiting the advantages of standardized construction in prefabricated structures. Second, replaceable energy dissipation elements are prone to fatigue failure under rare earthquakes, and their premature failure can aggravate the second-order effect ($P-\Delta$ effect) of gravity on the structural system. Therefore, an in-depth study of the cooperative working mechanisms between the structural parameters and material properties of energy dissipation elements in beam-column joints is necessary.

In order to address the aforementioned challenges, this study proposes a beam-column joint with a replaceable SEDBSs by integrating embedded CFRP circular tube concrete-filled square steel tube (CFSST) column [31], as shown in Fig. 1. This joint incorporates EDASCs as a centralized energy-dissipating component, enabling rapid post-earthquake functional recovery through the replacement of only these elements, thereby substantially reducing repair time and costs. In this study, the general-purpose finite element software ABAQUS is employed to develop a numerical model of the joint, whose accuracy is validated against representative experimental data. Parametric analyses are conducted to evaluate the influence of key parameters on the seismic performance of the joint and on the effectiveness of the "structural fuse" mechanism, leading to practical recommendations for structural optimization that can serve as a reference for the engineering application of resilient and recoverable structural systems.

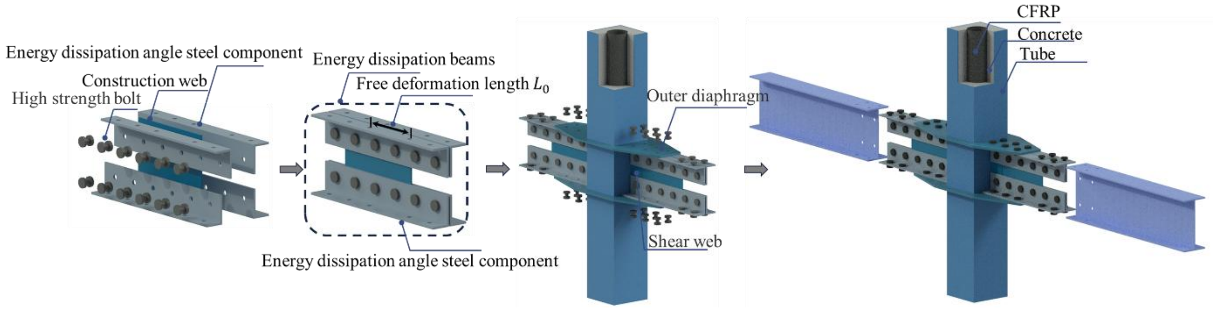

Fig. 1 Schematic diagram of the joint installation process

2. FE modeling and experimental verification

2.1. Joints design

The joint structure consists of an embedded CFRP circular tube CFSST with outer diaphragms and shear webs, a SEDBSs composed of EDASCs and constructed webs, and an H-beam, as shown in Fig. 1. All components are prefabricated in the factory. At the construction site, the assembly of the SEDBSs is completed first. Then, they are connected to the outer diaphragm and shear webs through full bolt connections to form a temporary support system. Finally, the overall hoisting of the H-beams is carried out. The installation is convenient and conducive to rapid disassembly and replacement after an earthquake. The research focuses on the side columns of the standard frame layer, and the beam-column dimensions are extracted from the inflection point of the prototype structure. The prototype structure is a 28-story, 106 m high aluminum alloy inner-core buckling-restrained brace (BRB)-embedded CFRP circular tube CFSST column structural system. The dimensions of the components in the model are as follows: the square steel tube column has a height of 1550 mm and a cross-sectional dimension of 250 mm × 250 mm × 8 mm; the H-beam has a cross-section of 300 mm × 150 mm × 6.5 mm × 9 mm. The inner diameter of the CFRP tube is 160 mm, consisting of three layers. A high-strength friction-type M20 bolt of grade 10.9 is used, with a preload force of 155 kN and a bolt hole diameter of 22 mm, as specified by the design values in the "GB 50017-2017 Standard for Steel Structure Design" [32]. Q355 steel is adopted for both the square steel tube and the H-beam, and the concrete strength grade is C50. The geometric configuration of the model is illustrated in Fig. 2.

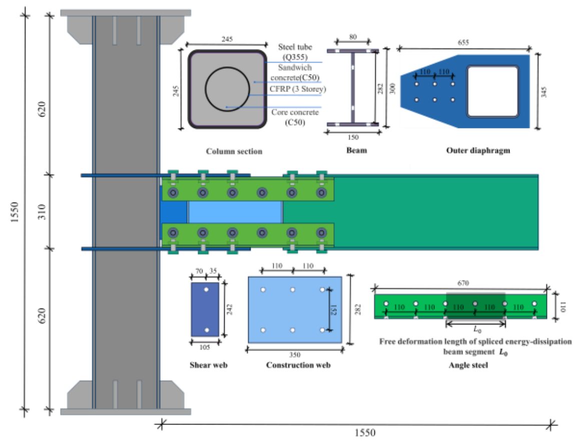

Fig. 2 Details dimensions of numerical models (mm)

2.2. Mechanism analysis

The design objectives of the embedded CFRP circular tube CFSST column-H-beam joint with energy-dissipation angle steel are as follows: (1) Under seismic loading, plastic damage is concentrated on the EDASCs, ensuring that the main structure remains elastic; (2) After an earthquake, the joint can be quickly repaired by replacing the EDASCs, and the seismic performance of the repaired joint is essentially the same as that of the undamaged joint. To achieve design goals and ensure that the EDASCs yields preferentially while dissipating energy intensively, it is necessary to satisfy the strength gradient control criterion: the plastic resistance bending moment of the EDASCs at the free deformation length of the SEDBSs must be smaller than that of outer diaphragm and beam. The design bearing capacity coefficient α_c is introduced to quantify this index, as shown in Eq. (1):

$$\alpha_c = \frac{M_{pl,fuse}}{M_{pl,beam}} \tag{1}$$

Where: $M_{pl,fuse}$ is the plastic resistance bending moment of EDASCs, $M_{pl,beam}$ is the plastic resistance bending moment of the whole section of the beam.

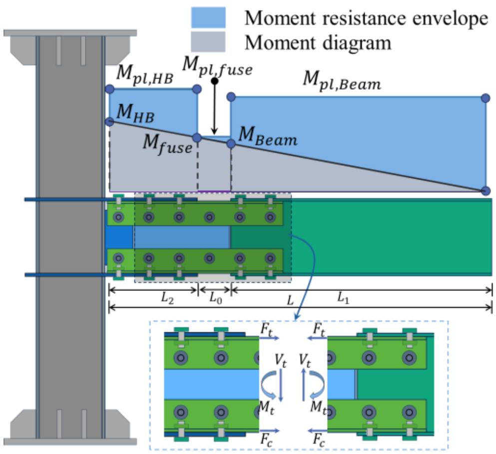

Fig. 3 Mechanism analysis of specimens

In Fig. 3, $M_{pl,HB}$ is the plastic resistance bending moment of the entire section at the connection between the outer diaphragm and the column flange, M_{HB} is the elastic resistance bending moment at the connection between the outer diaphragm and the column flange, M_{fuse} is the elastic resistance bending moment of the EDASCs at the free deformation length of the SEDBSs, and M_{Beam} is the elastic resistance bending moment of the beam. The plastic resistance bending moment of the EDASCs is equivalent to a pair of couple formed by the tension and compression in the upper and lower EDASCs, and the force analysis is shown in Fig. 3. $M_{pl,fuse}$ and $M_{pl,beam}$ can be calculated by Eqs. (2) and (3).

$$M_{pl,fuse} = W_{fuse} f_{y,a} \tag{2}$$

Where: $f_{y,a}$ is the yield strength of EDASCs, W_{fuse} is the elastic section modulus of free deformation length of the SEDBSs.

$$M_{pl,Beam} = W_{Beam} f_{y,Beam} \tag{3}$$

Where: W_{Beam} is the elastic section modulus of beam, $f_{y,Beam}$ is the yield strength of beam.

To ensure the "structural fuse" function of the joint, the following strength criteria must be satisfied: (1) The plastic resistance bending moment at the connection between the outer diaphragm and the column flange, as well as the plastic resistance bending moment of the entire interface of the beam, should be greater than their respective elastic resistance bending moments; (2) The plastic resistance bending moment of the EDASCs should be less than its elastic resistance bending moment. The above parameters can be calculated by Eqs. (4)-(6):

$$M_{pl,HB} > M_{HB} = P(L_1 + L_0 + L_2) \tag{4}$$

$$M_{pl,Beam} > M_{Beam} = PL_1 \tag{5}$$

$$M_{pl,fuse} < M_{fuse} = P(L_1 + L_0) \tag{6}$$

Where: L_0 is the free deformation length of the spliced link, L_1 is the length of the beam, L_2 is the length from the end of the outer diaphragm to the column flange.

2.3. Unit selection and constitutive relation

The mesh division and boundary conditions of the model are shown in Fig. 4. The CFRP circular tube is modeled using the reduced-integration 4-node shell element (S4R), In the thickness direction of the shell, three Simpson integration points are adopted. The other components adopt the 8-node hexahedron linear reduced-integration element (C3D8R). The grid size of the beam-column members in both the joint area and the non-joint area is 5 mm; To simulate the lateral restraint provided by the floor slabs and secondary beams to the main beams in the frame and prevent the steel beams from experiencing out-of-plane instability, lateral constraints (Limit its displacement in X and Y directions and rotation in X and Z directions) are applied to the steel beams, while Z-direction displacement is released at the top of the column to apply an axial force with an axial compression ratio of 0.3.

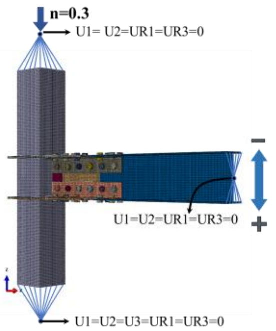

Fig. 4 Boundary conditions and meshing

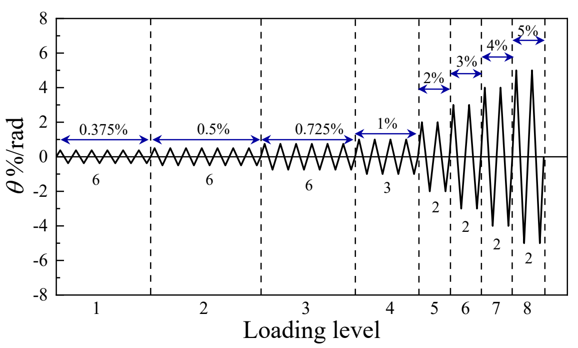

Fig. 5 Loading system

The constitutive relation of concrete adopts a plastic damage model considering the constraint effect of the steel tube, while that of steel adopts a five-segment linear model considering the strengthening section [33]. The CDP model parameters are shown in Table 1. The number of layers of CFRP circular tubes and direction of fiber stress are defined by the composite layer. The elastic-stage stress behavior is simulated using the Lamina model, while brittle fracture behavior at ultimate load is simulated using the Hashin damage function. The basic parameters of CFRP materials are shown in Table 2. The constitutive relation curve of high-strength bolts adopts a multi-linear isotropic hardening model, and bolt strength is calculated according to the standard GB/T 3098.1-2010 [34].

Table 1
CDP model parameters

Dilation Angle	Eccentricity	f_{bo}/f_{co}	K	Viscosity Parameter
40	0.1	1.2	0.6667	0.0005

Table 2
Basic parameters of CFRP materials

Thickness of single-layer CFRP (mm)	Ultimate tensile strength (MPa)	ν	E (GPa)
0.167	4200	0.304	283

2.4. Contact relationship and loading system

The failure mode of the joint is characterized by the formation of a plastic hinge in the SEDBSs. The beam-end loading method is beneficial for studying the seismic performance of the side-column joint model. Reciprocal displacement loading is applied at the beam end, following the provisions outlined in the Seismic Provisions for Structural Steel Buildings (ANSI/AISC 341-10) [35]. The maximum interlayer displacement angle is set to 5%, satisfying the AISC 341-10 requirement that the maximum plastic rotation angle for high-ductility joints be no less than 0.04 rad. The loading system is presented in Fig. 5.

Under low-cycle reciprocating loading at the beam end, friction occurs between the bolt head and the steel plate, while the bolt shank and the hole wall undergo continuous bearing and separation under cyclic loading. Therefore, the normal contact interaction between the bolt and the steel plate is defined as “hard” contact, with a tangential friction coefficient of 0.45. The tangential interaction between the concrete and the steel tube wall is assigned a friction coefficient of 0.60. Tie constraints are applied at the welded joints to simulate full continuity. Based on the coordinated deformation behavior of CFRP and concrete [36], the two materials are connected using tie constraints to ensure displacement compatibility.

2.5. FE verification of embedded CFRP circular tube CFSST column

This research employs the proposed modeling method to analyze specimen 1200-5-2 from the referenced literature [36], with the computational results juxtaposed against the experimental findings, as illustrated in Fig. 6. The finite element analytical curve aligns well with the test curve, exhibiting a peak bearing capacity discrepancy of 1.77%. Both the experimental specimens and those from finite element simulations exhibited drum-shaped failure. This work presents a modeling method that exhibits remarkable accuracy in simulating CFSST columns with embedded CFRP circular tubes.

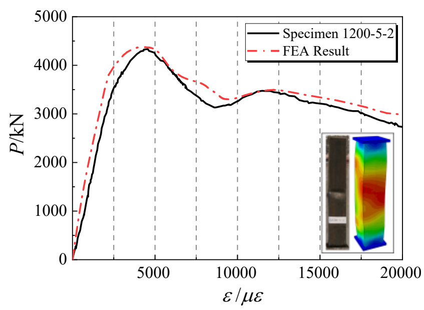

Fig. 6 1200–5-2 load-strain curves comparison

2.6. FE verification of joint

The specimen JD-2 in reference [37] was modeled using the method proposed in this paper. The comparison between the calculation results and the test results is shown in Fig. 7(a). During the test, the shear force generated at the connection between the outer diaphragms and the beam flange exceeded the preload of the high-strength bolts, causing bolt slippage and resulting in a distinct pinching effect in the hysteretic curve. Since the finite-element model did not explicitly simulate the slippage behavior between the bolts and the hole walls, the joint exhibited a higher overall stiffness at the initial stage of loading, leading to a weaker pinching effect and a relatively higher yield load in the calculated hysteretic curve. Despite this, the failure mode was highly consistent between the test and the finite-element modeling: local buckling occurred at the weak section of the beam flange, and significant plastic deformation was observed around the bolt holes. Additionally, although there was a 19.8% difference in the yield load, the difference in peak bearing capacity was only 3.8%, indicating that the modeling method has high accuracy in simulating the peak bearing capacity performance of this joint.

The specimen RT-2 from reference [38] was modeled using the numerical modeling approach proposed in this paper. A comparison between the calculated and experimental results is presented in Fig. 7(b). In terms of failure mode, both the test and the finite element simulation exhibit consistent behavior: the cantilever and mid-span segments of the steel beam remain elastic, while plastic deformation is localized in the web of the T-shaped steel section. The yield load differs by 12.4%, and the peak bearing capacity differs by 4.7%, indicating that the discrepancies at key characteristic points are relatively small.

The specimen PRBS in reference [39] was modeled using the method proposed in this paper. The comparison between the calculation results and the test results is shown in Fig. 7(c). From the failure mode, both the test and the finite element simulation show the same failure mode: the dog-bone-shaped beam section near the cantilever beam side flange buckles. The difference in the yield load is 6.2%, and the difference in the peak bearing capacity is 9.3%, indicating that the error of the characteristic points is relatively small. In summary, the proposed simulation method has good accuracy in simulating such nodes.

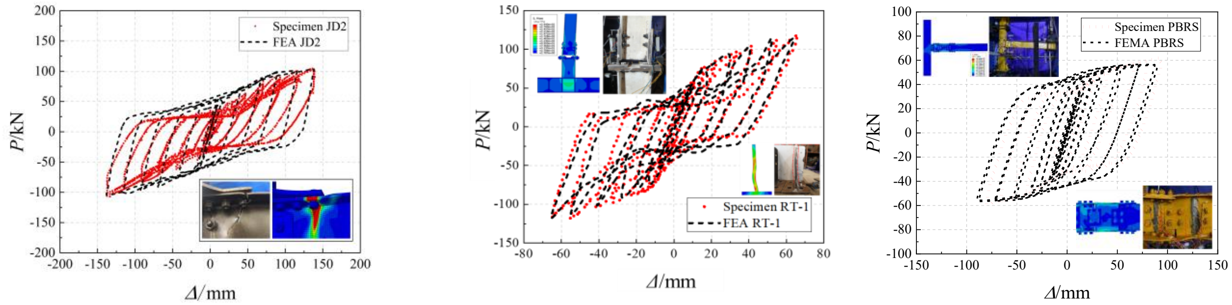

(a) Group 1 **(b) Group 2** **(c) Group 3**

Fig. 7 Joints hysteresis curve comparison

3. FE analysis of material with different EDASCs

This study builds three comparison models (JD0 series) using LY160, Q235, and Q355 steels to elucidate the impact of the material strength of EDASCs on the damage control mechanism and seismic performance of joints. These models are developed under the premise of an equal design bearing capacity coefficient ($\alpha_c = 0.83$) and a fixed free deformation length of the SEDBSs (L_0=1.5b_f). The geometric parameters of the EDASCs for each model are determined based on an equivalent criterion of material strength and thickness, ensuring that EDASCs with different material strengths possess the same bending resistance capacity. Detailed parameters for each model are presented in Table 3.

Table 3
JD0 series specimen parameters

Specimen	material strength	L_0	α_c	b_{JG}/mm
JD0-AS1	LY160	1.5b_f	0.83	13
JD0-AS2	Q235	1.5b_f	0.83	8
JD0-AS3	Q355	1.5b_f	0.83	5

Note: α_c is design resistance capacity coefficient; b_{JG} is EDASCs thickness; b_f is beam flange width; L_0 is free deformation length.

Fig. 8 shows the hysteresis curve of the JD0 series model. The abscissa is the interlayer displacement angle θ, and the ordinate is the actual bearing capacity coefficient α_r of the beam end. The expression is as follows:

$$\alpha_r = \frac{M_r}{M_{pl,beam}} \tag{7}$$

Where: M_r is the actual bending moment of the beam end, which equals to the product of the beam end load(P) and the beam length(L), $M_{pl,\ beam}$ is the plastic resistance bending moment of the entire beam section.

As illustrated in Fig. 8, the peak values of the actual bearing capacity coefficients for the JD0-AS1 and JD0-AS2 models are 1.59 and 1.58, respectively, significantly higher than the design bearing capacity coefficients of the joints ($\alpha_c = 0.83$). However, the actual bearing capacity coefficient of the JD0-AS3 model is 1.34, although slightly higher than the design bearing capacity coefficient, the bearing capacity significantly degrades once the interlayer displacement angle exceeds 3%.

The characteristic parameters of the skeleton curve for JD0 series models are consolidated in Table 4. With the same design bearing capacity coefficient, the thickness of the JD0-AS3 model is reduced due to the enhanced material strength of the EDASCs. The initial rotational stiffness (K_0) of the JD0-AS3 model is 19.15% and 10.74% inferior to that of the JD0-AS1 and JD0-AS2 models, respectively, while the ductility (μ) is diminished by 36.78% and 30.71%. It can be deduced that maintaining a consistent design bearing capacity coefficient while enhancing the material strength of the EDASCs substantially diminishes the joint's initial rotational stiffness, bearing capacity, and deformation capacity.

Fig. 9 shows the calculation method for the local hysteresis curve of the EDASCs. The abscissa Δ is the tensile and compressive displacement at point A on the upper flange of the EDASCs, while the ordinate F is the equivalent axial force of the $a - a$` section of the EDASCs. To reveal the working mechanism of the EDASCs as a "structural fuse", the local hysteresis curve is extracted, as shown in Fig. 10. Under reciprocating loads applied at the beam end, the EDASCs experiences positive tension elongation and negative compression buckling. In the elastic stage, the positive and negative displacements of the hysteresis curve are symmetrical, and the relationship between the equivalent axial force and displacement is linear, indicating that the EDASCs remains in a linear elastic state without cumulative damage. In the plastic stage, however, the effective bearing area decreases due to buckling deformation under compression, leading to significant pinching of the hysteresis curve.

In summary, the synergistic effect of material strength and thickness of EDASCs is critical for regulating the function of the "structural fuse". When the ratio of the actual bearing capacity coefficient of the joint to the design bearing capacity coefficient approaches 1, the safety margin of the joint decreases, and the buckling deformation of the flange of the EDASCs increases, resulting in a deterioration of the joint's bearing capacity and a significant reduction in its deformation capacity. The "structural fuse" function fails earlier than expected.

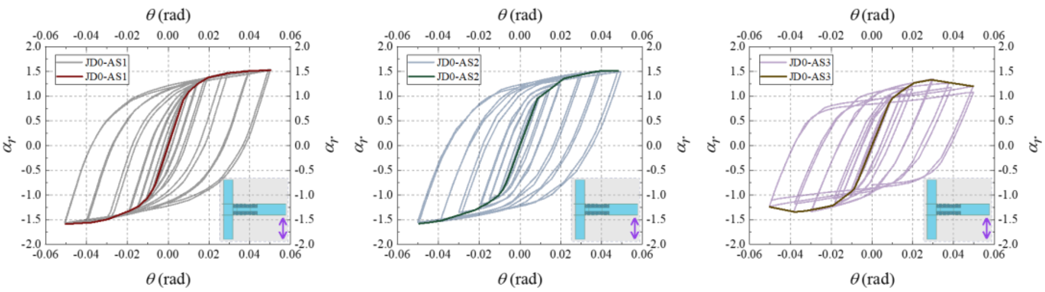

Fig. 8 Comparison of the global hysteresis curves of joints

Table 4
Summary of characteristic parameters of skeleton curves

Specimen	K_0（kN•m/rad）	α_r	α_c	α_r/α_c	μ
JD0-AS1	19812.01	1.59	0.83	1.92	5.71
JD0-AS2	17945.39	1.58	0.83	1.90	5.21
JD0-AS3	16018.57	1.34	0.83	1.61	3.61

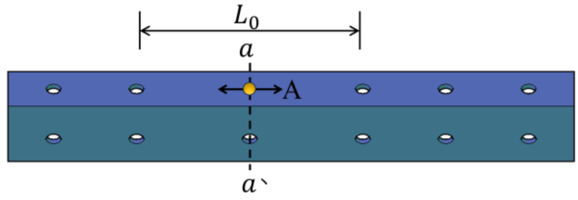

Fig. 9 Calculation method of horizontal and vertical coordinates for local hysteresis curves

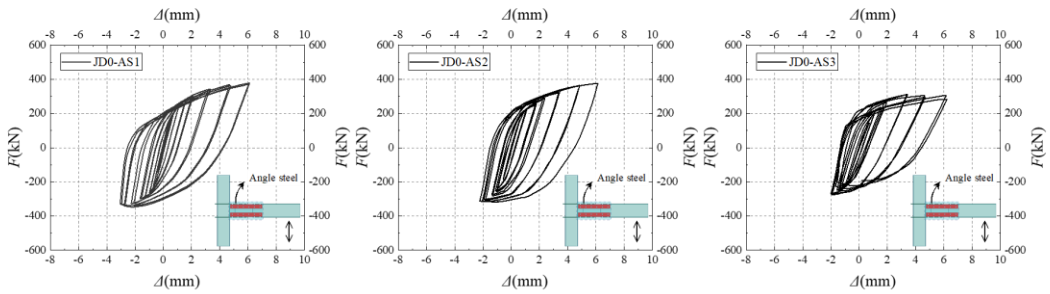

Fig. 10 Comparison of the local hysteresis curves of EDASCs

Fig. 11 shows the ratio of the total energy dissipation of each component to that of the joint model. In the post-processing module of the ABAQUS software, extract the ALLPD (plastic energy dissipation) values of each component. In Fig. 11, E_D, E_{JG}, E_{HB}, E_{H}, E_{FB}, E_{JQB}, and E_{C} correspond to the energy dissipation values of the entire joint, EDASCs, outer diaphragm, beam, constructed webs, shear web and column respectively. As shown in Fig. 11, during the elastic stage, the total energy dissipation of the column (E_{C}) and the EDASCs (E_{JG}) is close to 100%. In the plastic stage, the EDASCs becomes the primary energy dissipation component. When the interlayer displacement angle reaches 5%, the energy dissipation ratio of the JD0-AS2 model's EDASCs increases to 98%, while that of the column decreases to 1.7%. Compared with models JD0-AS1 and JD0-AS3, the energy dissipation of the JD0-AS2 model's EDASCs increases by 11.34% and 8.16%, respectively. Fig. 12 shows a comparison of each component's cumulative energy dissipation capacity. JD0-AS2 model's cumulative energy dissipation value is 87.85 kN•m, which is higher than those of JD0-AS1 (E_D= 81.24 kN•m) and JD0-AS3 (E_D= 80.39 kN•m) by 8.13% and 9.28%, respectively.

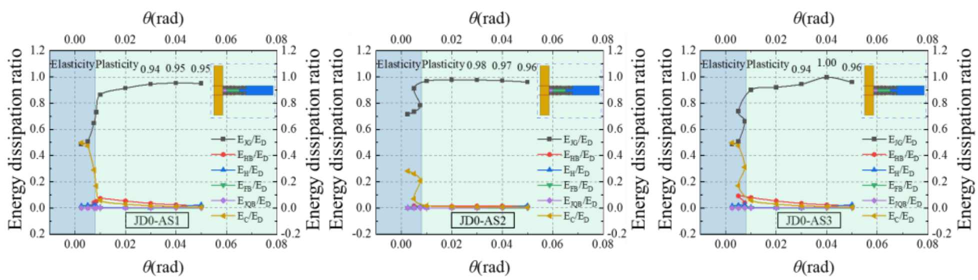

Fig. 11 Energy dissipation ratio

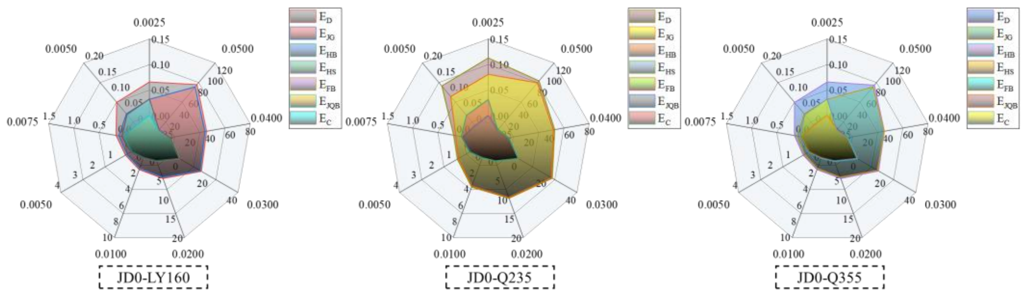

Fig. 12 Cumulative energy dissipation

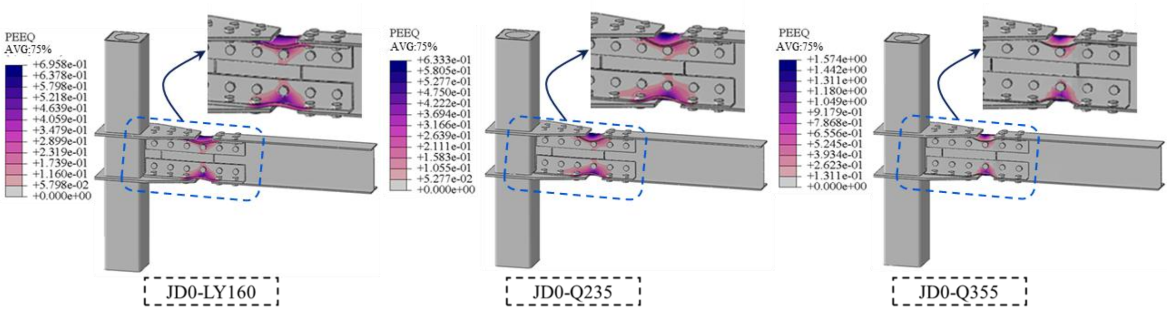

Fig. 13 Damage distributions

Fig. 13 shows the equivalent plastic strain (PEEQ) distribution of each joint model. Under the same design bearing capacity coefficient ($\alpha_c = 0.83$), the plastic damage in the joint is primarily concentrated on the EDASCs, while the remaining components are in elastic state. In summary, the synergistic effect of material strength and thickness of EDASCs significantly influences the seismic performance of joints. Although the LY160 steel has features such as a low yield point and high ductility, which are conducive to enhancing the energy dissipation capacity of the joint, its relatively low yield strength leads to a relatively lower ultimate bearing capacity of the joint. However, the joints using EDASCs made of Q235 steel not only have good ductility and stable energy dissipation capacity, but also exhibit higher ultimate bearing capacity and stiffness reserve, which is more in line with the optimization design principle of this paper aiming at “structural fuse” function and seismic performance. Therefore, Q235 steel is a better choice that takes both performance and cost into account.

4. Parameter analysis

According to the study results in Section 3, Q235 steel has been chosen for the EDASCs. In this section, the design bearing capacity coefficient and the free deformation length of the SEDBSs are identified as the primary parameters. These parameters are used to examine their effects on the “structural fuse” function and seismic performance of the embedded CFRP circular tube CFSST column-H-beam joint with energy-dissipation angle steel.

4.1. Parameter design

The design bearing capacity coefficient α_c is used to characterize the weakening degree of EDASCs, with α_c values set at 0.58, 0.66, 0.75, 0.83, 0.98, and 1.19, respectively. The free deformation length of the SEDBSs is set to be 1, 1.5, and 2 times the width of the beam flange. The length of EDASCs are 610 mm, 670 mm, and 750 mm respectively, corresponding to free deformation lengths of 160 mm, 220 mm, and 300 mm as shown in Fig. 14. The specific parameters of each model are shown in Table 5. The “JD-AS” double parameter number is used: the JD series characterizes the free deformation length of different SEDBSs, while the AS series characterizes different design bearing capacity coefficients. A total of 18 groups of models were established. The loading system, material properties and boundary conditions are consistent with those described in Section 3.

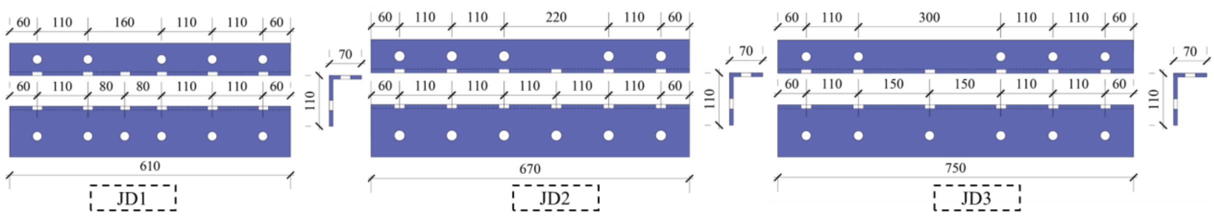

Fig. 14 Detail dimensions of EDASCs (mm)

Table 5
Numbers and main parameters of joint models

Specimen	L_0/b_f	b_{JG}/mm	α_c
JD1-AS1	1	5	0.58
JD1-AS2		6	0.66
JD1-AS3		7	0.75
JD1-AS4		8	0.83
JD1-AS5		10	0.98
JD1-AS6		13	1.19
JD2-AS1	1.5	5	0.58
JD2-AS2		6	0.66
JD2-AS3		7	0.75
JD2-AS4		8	0.83
JD2-AS5		10	0.98
JD2-AS6		13	1.19
JD3-AS1	2	5	0.58
JD3-AS2		6	0.66
JD3-AS3		7	0.75
JD3-AS4		8	0.83
JD3-AS5		10	0.98
JD3-AS6		13	1.19

4.2. Overall hysteresis responses

Fig. 15 shows the hysteresis curves of the joint models. As the design bearing capacity coefficient increases, the shape of the hysteresis loops gradually transitions from "rectangular" to "shuttle-like," indicating improved stability and reduced degradation of the joint's load-carrying capacity under cyclic loading. Table 6 summarizes the characteristic parameters of the skeleton curves for each model. The actual bearing capacity coefficient exceeds its design value, and the ratio of actual to design bearing capacity coefficient first increases and then decreases with increasing design coefficient. The maximum ratio is observed in the JD-AS4 model among the JD series.

Since the hysteresis curve of the joint does not exhibit obvious stiffness degradation, the shape change specific energy theory is applied to compare the ductility of each specimen. According to this theory, material damage occurs when the shape change ratio at any location within the specimen reaches its limit value under unidirectional stress. As shown in Table 6, the displacement ductility coefficient of the joint ranges from 3.16 to 6.36, indicating a significant capacity for deformation. When the free deformation length of the SEDBSs at the joint remains constant, an increase in the design bearing capacity coefficient leads to greater EDASC thickness, reduced joint deformation capacity, and higher initial rotational stiffness. Conversely, with a constant design bearing capacity coefficient, increasing the free deformation length of the SEDBSs results in lower initial rotational stiffness and a non-monotonic variation in ductility first increasing and then decreasing. Clearly, both the design bearing capacity coefficient and the free deformation length of the SEDBSs have significant effects on the joint's ductility and initial rotational stiffness. To prevent out-of-plane instability due to excessive weakening, a lower bound should be established for the design bearing capacity coefficient. Moreover, an upper bound for the free deformation length of the SEDBSs is necessary to achieve an optimal balance between the "structural fuse" function and the seismic performance of the joint.

According to American standard ANSI/AISC 360-22 [40] and European standard EC3 [41], joints are classified according to the initial rotational stiffness. For connection joints without support structure, when the initial rotational stiffness K_0 of the joints satisfies (0.5-25) EI/L, it is proven to be classified as semi-rigid joints. The calculated initial rotational stiffness of all joint models falls within the range of (1.42-2.27) EI/L, confirming their classification as semi-rigid joints.

Table 6
Skeleton curve characteristic parameter summary

Specimen	K_0（kN•m/rad）	$\frac{K_0}{EI/L}$	Category	α_r	α_c	α_r/α_c	μ
JD1-AS1	17742.80	1.82	Semi-rigid	1.03	0.58	1.78	6.36
JD1-AS2	18606.40	1.90		1.24	0.66	1.88	6.27
JD1-AS3	19525.47	2.00		1.46	0.75	1.95	5.77
JD1-AS4	20011.35	2.05		1.67	0.83	2.01	5.46
JD1-AS5	21289.74	2.18		1.82	0.98	1.86	5.11
JD1-AS6	22191.64	2.27		2.09	1.19	1.76	3.41
JD2-AS1	15758.36	1.61		0.97	0.58	1.67	6.47
JD2-AS2	16934.95	1.73		1.20	0.66	1.82	6.35
JD2-AS3	17444.27	1.79		1.37	0.75	1.83	5.79
JD2-AS4	17945.39	1.84		1.58	0.83	1.90	5.47
JD2-AS5	19273.30	1.97		1.73	0.98	1.77	5.20
JD2-AS6	20138.60	2.06		2.01	1.19	1.69	3.57
JD3-AS1	13889.75	1.42		0.89	0.58	1.53	6.23
JD3-AS2	14800.05	1.51		1.09	0.66	1.65	5.39
JD3-AS3	16450.54	1.68		1.47	0.75	1.96	5.23
JD3-AS4	16604.23	1.70		1.31	0.83	1.58	5.11
JD3-AS5	17328.07	1.77		1.64	0.98	1.67	4.66
JD3-AS6	17975.37	1.84		1.88	1.19	1.58	3.16

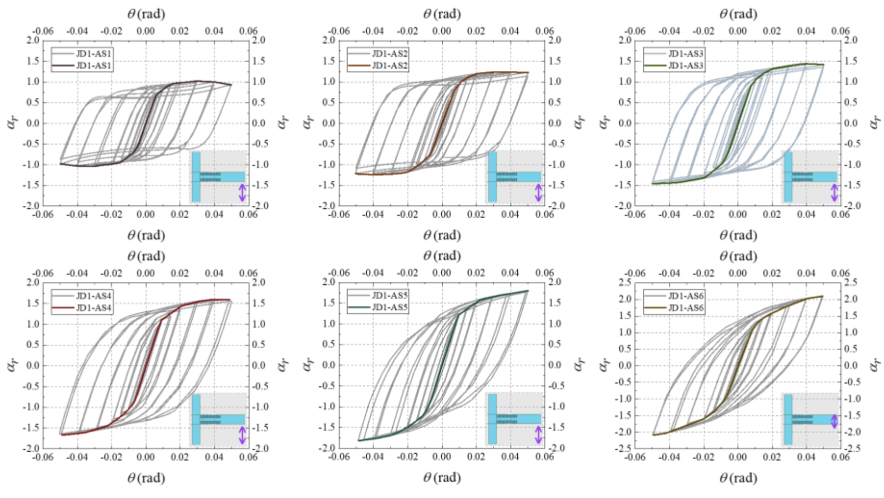

(a) $L_0/b_f = 1$, JD1 series

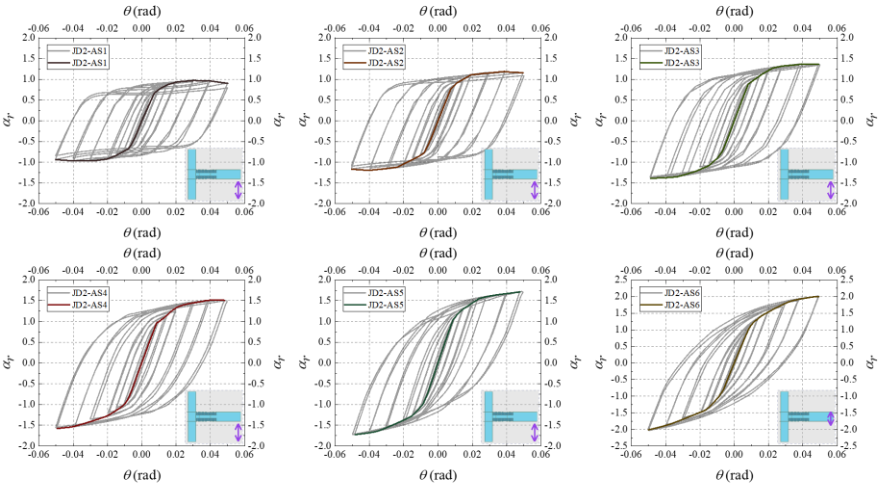

(b) $L_0/b_f = 1.5$, JD2 series

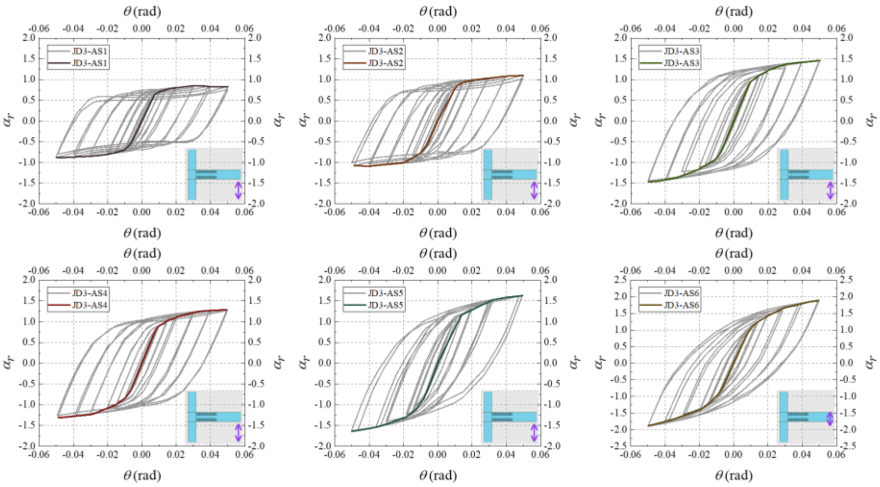

(c) $L_0/b_f = 2$, JD3 series

Fig. 15 Comparison of the global hysteresis curves of joints

4.3. EDASCs hysteresis responses

To analyze the working mechanism of EDASCs, the local hysteresis curves of these components in each model are extracted, as shown in Fig. 16. In the elastic stage, positive and negative tension and compression are symmetrically distributed; in the plastic stage, a significant pinching effect occurs. This is because the EDASCs does not yield in the elastic stage, maintaining consistent positive and negative tension and compression deformation. In the plastic stage, the EDASCs is elongated under positive tension, resulting in a full hysteresis curve with good energy dissipation capacity. Under negative compression, buckling deformation occurs in the EDASCs, leading to reduced compressive deformation displacement and decreased energy dissipation capacity.

Under the condition of a constant free deformation length of the spliced link, as the design bearing capacity coefficient increases, the weakening of the EDASCs decreases, while the compression deformation of the EDASCs increases. This results in an increased proportion of the load transmitted from the bolt to the outer diaphragm, thereby weakening the "structural fuse" function. When the design bearing capacity coefficient is consistent, increasing the free deformation length of the spliced link has minimal influence on the mechanical properties of the EDASCs.

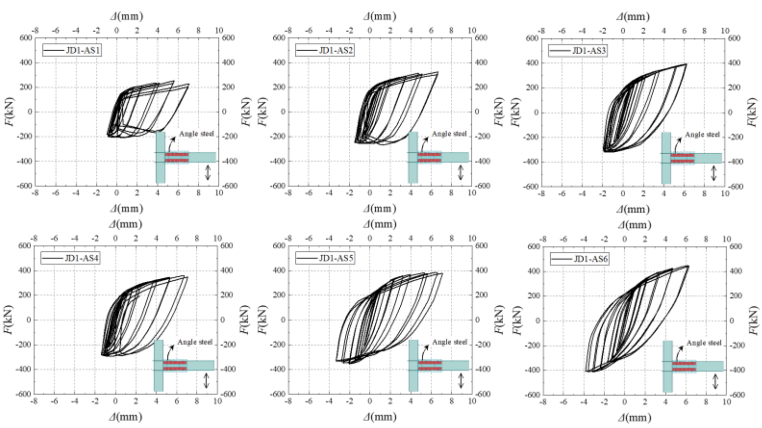

(a) $L_0/b_f = 1$, JD1 series

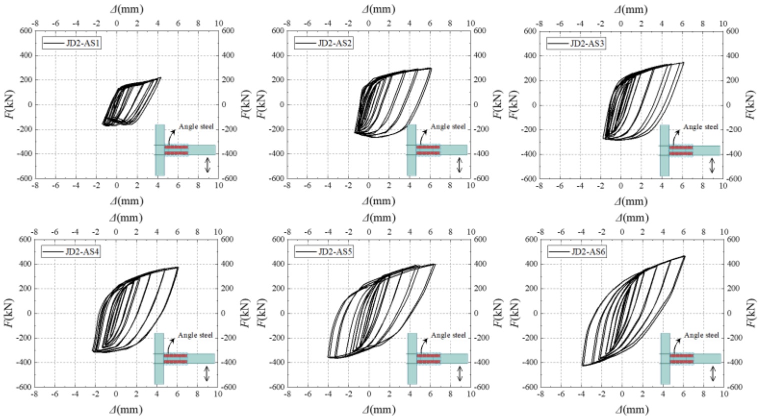

(b) $L_0/b_f = 1.5$, JD2 series

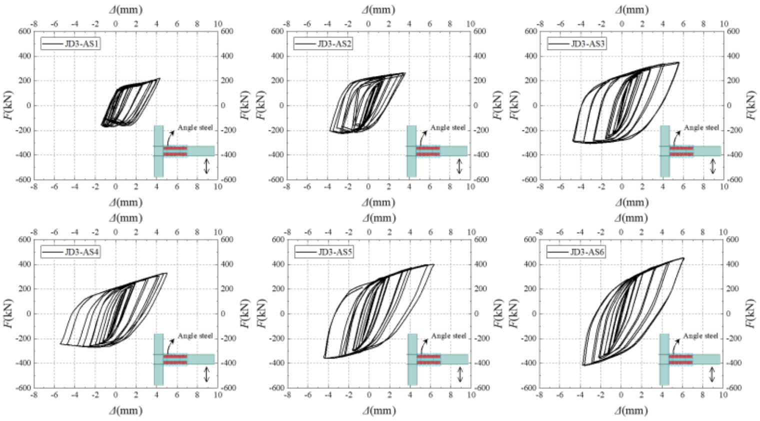

(c) $L_0/b_f = 2$, JD3 series

Fig. 16 Comparison of the local hysteresis curves of EDASCs

4.4. Energy dissipation ratio

The ratio of the energy dissipation of each component to the total energy dissipation of the joint under each displacement loading amplitude is extracted to quantitatively evaluate the "structural fuse" function of the EDASCs, as shown in Fig. 17. In the post-processing module of the ABAQUS software, extract the ALLPD (plastic energy dissipation) values of each component. In the elastic stage, energy dissipation is shared between column and the EDASCs; in the plastic stage, energy dissipation is primarily borne by the EDASCs, while the contribution of the column decreases. When the design bearing capacity coefficient is less than 0.75, the energy dissipation ratio of the EDASCs reaches 90%-100% under an interlayer displacement angle of 5%, effectively realizing the "structural fuse" function. When the design bearing capacity coefficient exceeds 0.98, the energy dissipation ratio of the EDASCs decreases to 70%-95%, while that of the outer diaphragms and column increases to 3%-24%. It has been demonstrated that when the design bearing capacity coefficient exceeds 0.98, plastic damage diffuses from the EDASCs to the outer diaphragms and the beam, causing irreversible plastic deformation in the main structure and weakening the "structural fuse" function of the EDASCs. Increasing the free deformation length of the spliced link increases the energy dissipation ratio of the EDASCs by less than 3%, indicating that the free deformation length of the spliced link has limited influence on the energy dissipation ratio of each component in the model.

In summary, an increase in the design bearing capacity coefficient is associated with a gradual decrease in the energy dissipation ratio of the EDASCs, while the energy dissipation ratio of the column and outer diaphragms gradually increases. This phenomenon observed in the experimental results leads to a weakening of the "structural fuse" function of the EDASCs. Therefore, it is necessary to establish an upper limit for the design bearing capacity coefficient. This will ensure that plastic damage is effectively concentrated on the EDASCs. Furthermore, the augmentation of the free deformation length of the SEDBSs exerts a negligible influence on the enhancement of the "structural fuse" function of the EDASCs.

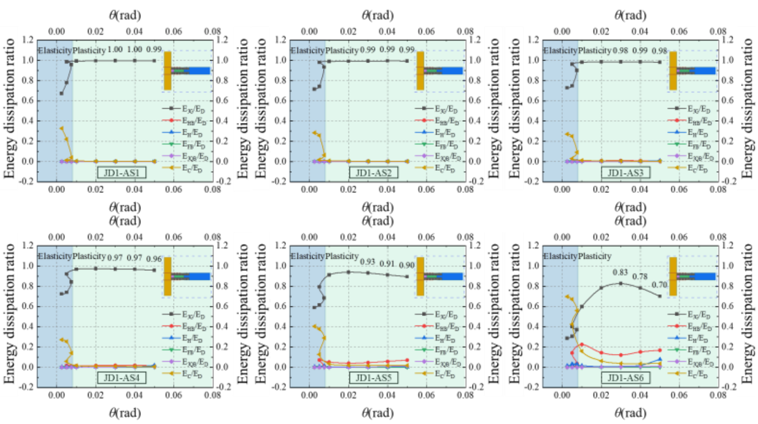

(a) $L_0/b_f = 1$, JD1 series

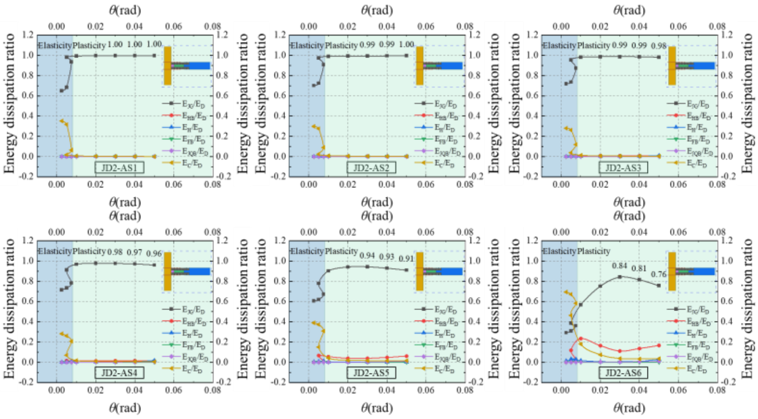

(b) $L_0/b_f = 1.5$, JD2 series

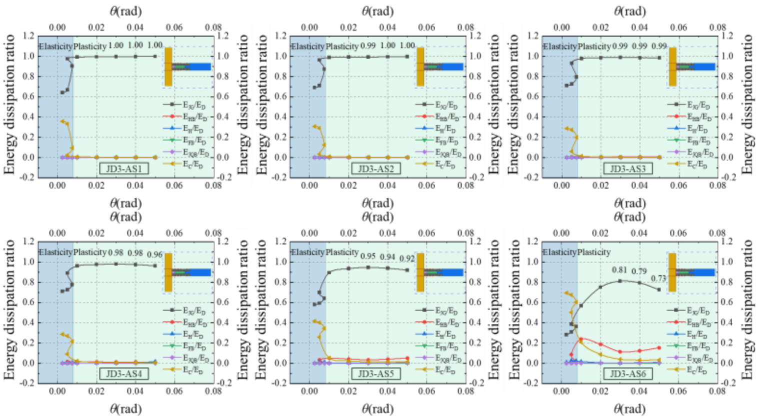

(c) $L_0/b_f = 2$, JD3 series

Fig. 17 Comparison of the energy dissipation ratio

4.5. Damage deformation distribution

Fig. 18 illustrates the distribution of equivalent plastic strain (PEEQ) across each model. A darker color indicates a higher level of accumulated plastic damage, reflecting the material's ductility and susceptibility to fracture. Thus, PEEQ serves as an effective index for evaluating the fracture potential of the steel. All EDASCs exhibit significant buckling deformation, with peak equivalent plastic strain localized within the EDASCs. When the design bearing capacity coefficient is below 0.75, reduced thickness of the EDASCs leads to pronounced buckling and diminished out-of-plane stability of the joint. Conversely, when the coefficient exceeds 0.98, the equivalent plastic strain in the EDASCs decreases, and the plastic hinge shifts away from the beam, outer diaphragms, and column flange connections, partially compromising the intended "structural fuse" behavior. Examination of the columns in Fig. 18 further shows that, under a constant design bearing capacity coefficient, increasing the free deformation length of the spliced link reduces the overall equivalent plastic strain level at the joint and promotes a more uniform distribution of damage within the EDASCs. This indicates that extending the free deformation length of the SEDBSs enhances control over damage localization in the EDASCs.

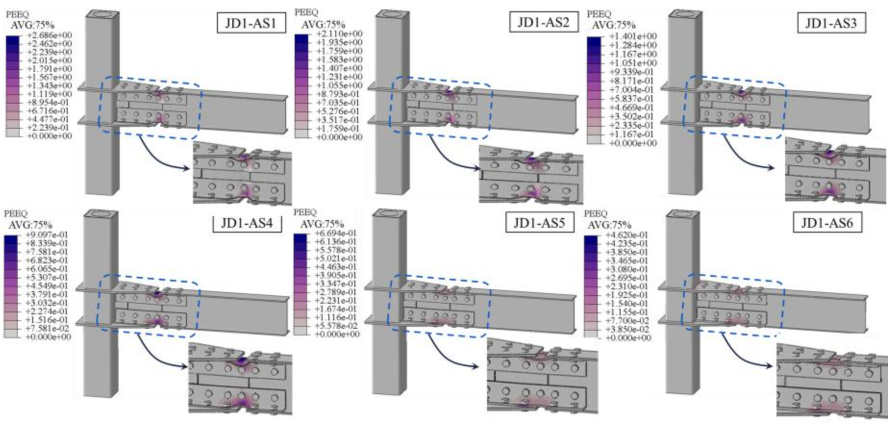

(a) $L_0/b_f = 1$, JD1 series

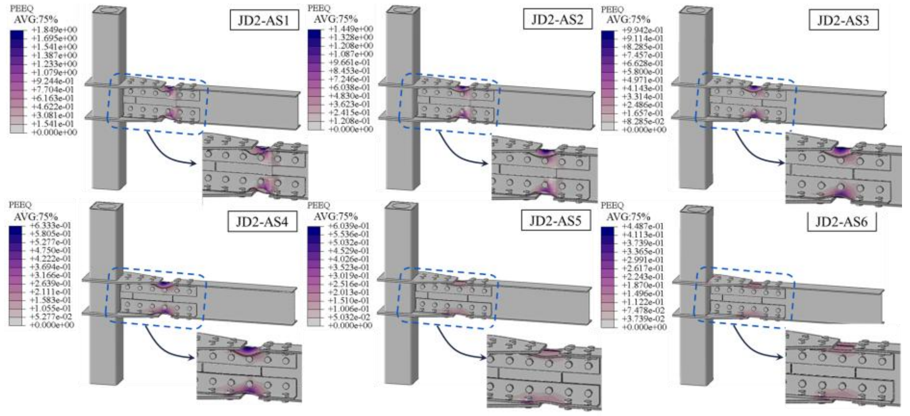

(b) L_0/b_f = 1.5, JD2 series

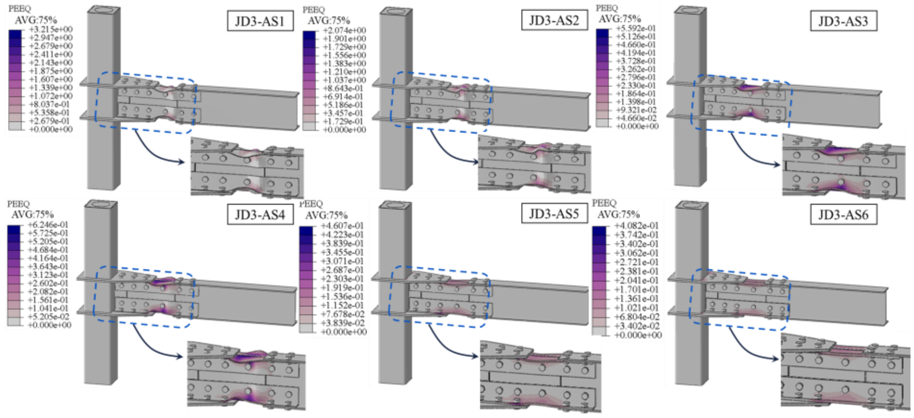

(c) L_0/b_f = 2, JD3 series

Fig. 18 Comparison of cumulative plastic strain distributions of joints

5. Optimal design suggestion

To attain the design objective of controllable joint damage and post-earthquake reparability, it is crucial to concentrate plastic deformation on the EDASCs. Based on the ratio of the total energy dissipation of the EDASCs, columns, outer diaphragms, and joints under a 5% interlayer displacement angle, combined with the analysis in Section 4, it can be observed that when the energy dissipation ratio of the outer diaphragms and columns exceeds 4% and the energy dissipation ratio of the EDASCs is less than 90%, plastic damage distribution diffuses from the EDASCs to the beam, outer diaphragms, and column flange connections. Consequently, the critical value serves as the effective threshold of the “structural fuse”, ensuring rapid restoration of functionality by replacing the EDASCs post-earthquake.

Fig. 19 illustrates the correlation between the energy dissipation ratio of each component, the design bearing capacity coefficient, and the free deformation length of the spliced link. The analysis of the energy dissipation ratio presented in Table 7 and Fig. 19 reveals the impact of the design bearing capacity coefficient and the free deformation length of the SEDBSs on the energy dissipation mechanism of the joint. At an interlayer displacement angle of 5%, when the design bearing capacity coefficient is below 0.75, the EDASCs is a thin-walled angle steel component, susceptible to significant out-of-plane buckling deformation, consequently diminishing the joint’s load-bearing capacity. When the design bearing capacity coefficient surpasses 0.98, the augmented strength of the EDASCs causes the joint's plastic degradation to propagate from the EDASCs to the beam and outer diaphragms. The energy dissipation ratio of the outer diaphragms rises to 5%-20%, resulting in the failure of the “structural fuse” function. With a consistent design bearing capacity coefficient, augmenting the free deformation length of the SEDBSs leads to variations of up to 3% in the energy dissipation ratios of the outer diaphragms and columns, and up to 5% in the energy dissipation ratio of the EDASCs.

In summary, considering the bearing capacity, initial rotational stiffness, ductility, “structural fuse” function, and material utilization rate of the joints, it is advisable to establish the design bearing capacity coefficient within the range of 0.75-0.98, and the free deformation length of the spliced link beam section should be 1-1.5 times the width of the beam flange. This design guarantees the preferential yielding of the EDASCs. By meticulously adjusting the design bearing capacity coefficient and the free deformation length of the SEDBSs, the design goals of “concentrated energy dissipation in the EDASCs, no damage in the main structure, and rapid replacement after an earthquake” can be achieved.

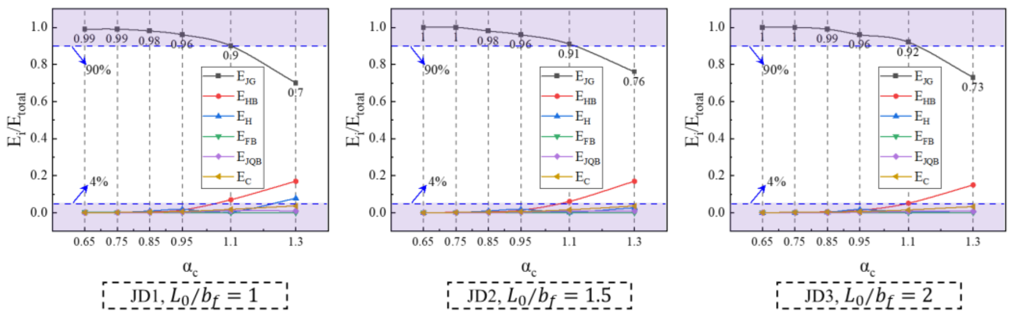

Fig. 19 The relationship between the proportion of component energy dissipation and key parameters

Table 7
Comparison of fuse effect of structure

Specimen	Energy proportion of EDASCs	Energy proportion of column	The proportion of energy dissipation of outer diaphragm	α_r/α_c	Plasticity concentration position
JD1-AS1	99.61%	0.14%	0	1.78	EDASCs
JD1-AS2	99.46%	0.18%	0.29%	1.88	EDASCs
JD1-AS3	98.51%	0.42%	0.81%	1.95	EDASCs
JD1-AS4	96.77%	0.79%	1.82%	2.01	EDASCs
JD1-AS5	91.31%	1.77%	5.76%	1.86	outer diaphragm, EDASCs
JD1-AS6	70.12%	3.65%	16.82%	1.76	outer diaphragm, EDASCs
JD2-AS1	99.82%	0.14%	0	1.67	EDASCs
JD2-AS2	99.51%	0.19%	0.28%	1.82	EDASCs
JD2-AS3	98.63%	0.42%	0.79%	1.83	EDASCs
JD2-AS4	97.18%	0.71%	1.57%	1.90	EDASCs
JD2-AS5	92.91%	1.54%	4.72%	1.77	outer diaphragm, EDASCs
JD2-AS6	75.68%	3.55%	16.59%	1.69	outer diaphragm, EDASCs
JD3-AS1	99.81%	0.15%	0	1.53	EDASCs
JD3-AS2	99.53%	0.22%	0.23%	1.65	EDASCs
JD3-AS3	98.71%	0.36%	0.62%	1.96	EDASCs
JD3-AS4	97.51%	1.28%	0.62%	1.58	EDASCs
JD3-AS5	93.85%	2.09%	3.99%	1.67	outer diaphragm, EDASCs
JD3-AS6	79.28%	3.27%	15.23%	1.58	outer diaphragm, EDASCs

6. Conclusions

This study investigated the seismic performance and "structural fuse" function of the embedded CFRP circular tube CFSST column-H-beam joint with energy-dissipation angle steel under reciprocating load using ABAQUS finite element analysis. The analysis focused on the influence of the material strengths of EDASCs, design bearing capacity coefficients, and free deformation lengths of SEDBSs on energy dissipation, initial rotational stiffness, and damage distribution, and provided optimized design recommendations. The main conclusions are as follows:

(1) Considering bearing capacity, initial rotational stiffness, and energy dissipation ratio of joints, it is suggested that the steel of EDASCs should be Q235, which can effectively balance the "structural fuse" function and seismic performance of beam-column joints. According to European standard EC3, The embedded CFRP circular tube CFSST column-H-beam joint with EDASCs is proven to be classified as a semi-rigid joint.

(2) As the design bearing capacity coefficient increases, the plastic damage distribution diffuses from the EDASCs to the outer diaphragm. The energy dissipation of the column and the outer diaphragm accounts for more than 5%, and the damage cannot be concentrated on the EDASCs. However, when the design bearing capacity coefficient is less than 0.75, the EDASCs is thin-walled, and obvious out-of-plane buckling deformation will occur under large deformation, resulting in serious bearing capacity degradation of the joint. It is suggested that the design bearing capacity coefficient of the joint should be 0.75-0.98.

(3) The increase of the free deformation length of the SEDBSs has a significant effect on the plastic damage distribution of the joint, but the improvement of the "structural fuse" function is limited. When the free deformation length of the SEDBSs exceeds 1.5 times the width of the beam flange, the buckling deformation of the EDASCs decreases, but the bearing capacity, initial rotational stiffness, ductility and energy dissipation capacity of the joint are significantly reduced. It is suggested that the free deformation length of the spliced link should be 1-1.5 times the width of the beam flange.

Acknowledgements

The authors acknowledge the financial support from Key Projects of the National Natural Science Foundation of China, China (No. 51938009), and the Natural Science Foundation of Shenyang, China (No. 23-503-6-09).

References

[1] Han L H. Concrete filled steel tubular structures: theory and practice[M]. 3rd ed. Beijing: Science Press, 2016 (in Chinese).
[2] Li G C, Zhang C Y, Yu H P. Advance in high-strength concrete filled square steel tubular structure with inner CFRP circular tube[J]. Engineering Mechanics, 2012, 29(2): 57-68 (in Chinese).
[3] Yang Z J, Li G C, Lang Y, et al. Flexural behavior of high strength concrete filled square steel tube with inner CFRP circular tube[J]. KSCE Journal of Civil Engineering, 2017, 21(7): 2728-2737.
[4] Yang Z, Li G, Lang Y, et al. Behavior of high strength concrete filled square steel tube stub columns with inner CFRP tube under biaxial eccentric compression[J]. Computer Modeling in Engineering & Sciences, 2021, 127(1): 273-290.
[5] Miller D K. Lessons learned from the Northridge earthquake[J]. Engineering Structures, 1998, 20(4-6): 249-260.
[6] Sofias C E, Pachoumis D T. Assessment of reduced beam section (RBS) moment connections subjected to cyclic loading[J]. Journal of Constructional Steel Research, 2020, 171: 106151.
[7] Castiglioni C A, Kanyilmaz A, Calado L. Experimental analysis of seismic resistant composite steel frames with dissipative devices[J]. Journal of Constructional Steel Research, 2012, 76: 1-12.
[8] Li S, Jiang H, Liu X. Seismic performance of earthquake resilient structure with replaceable components[J]. Journal of Building Engineering, 2025, 99: 111597.
[9] Lu X L, Wu D Y, Zhou Y. State-of-the-art of earthquake resilient structures[J]. Journal of Building Structures, 2019, 40(2): 1-15 (in Chinese).
[10] Zhang Q, Men J, Wu X, et al. Demountable and replaceable performance evaluation of a novel bolts-flange connected RC column[J]. Structures, 2024, 70: 107894.
[11] Shoeibi S, Kafi M A, Gholhaki M. New performance-based seismic design method for structures with structural fuse system[J]. Engineering Structures, 2017, 132: 745-760.
[12] Oh K, So J, Ha H, et al. Seismic performance evaluation of Korean column-tree steel moment connections[J]. International Journal of Steel Structures, 2016, 16: 1287-1298.
[13] Zhang Y X, Liu A, Zhang A L, et al. Seismic performance analysis of a resilient prestressed steel frame with intermediate column containing friction dampers[J]. Advanced Steel Construction, 2017, 13(3): 241-257.
[14] Hou H, Li H, Qiu C, et al. Effect of hysteretic properties of SMA s on seismic behavior of self-centering concentrically braced frames[J]. Structural Control and Health Monitoring, 2018, 25(3): e2110.
[15] Köroğlu M A, Köken A, Dere Y. Use of different shaped steel slit dampers in beam to column connections of steel frames under cycling loading[J]. Advanced Steel Construction, 2018, 14(2): 251-273.
[16] Tong C, Wu J, Li C. A novel precast concrete beam-to-column connection with replaceable energy-dissipation connector: Experimental investigation and theoretical analysis[J]. Bulletin of Earthquake Engineering, 2021, 19(12): 4911-4943.
[17] Zhang A L, Li S H, Jiang Z Q, et al. Design theory of earthquake-resilient prefabricated sinusoidal corrugated web beam-column joint[J]. Engineering Structures, 2017, 150: 665-673.
[18] Jiang Z Q, Chen M L, Yang Z S, et al. Cyclic loading tests of self-centering prestressed prefabricated steel beam-column joint with weakened FCP[J]. Engineering Structures, 2022, 252: 113578.
[19] Lu B, Zhao B, Wang C, et al. Experimental study on seismic behavior of replaceable energy dissipation braces with square steel tubes and rectangular steel plates[J]. Structures, 2025, 73: 108409.
[20] Zhang X, Zhou B, Gao J D, et al. Numerical investigation on seismic performance of prefabricated steel beam-to-column connection with replaceable U-shaped plate[J]. Advanced Steel Construction, 2024, 20(4): 7-405.
[21] Zhao L Y, Guo D, Yang Y Q, et al. Seismic performance and replaceability of steel frame structures with replaceable beam segments[J]. Advanced Steel Construction, 2024, 20(1): 69-80.
[22] Chou C C, Wu C C. Performance evaluation of steel reduced flange plate moment

connections[J]. Earthquake engineering & structural dynamics, 2007, 36(14): 2083-2097.
[23] Calado L, Proença J M, Espinha M, et al. Hysteretic behaviour of dissipative bolted fuses for earthquake resistant steel frames[J]. Journal of Constructional Steel Research, 2013, 85: 151-162.
[24] He X, Chen Y, Eatherton M R, et al. Experimental evaluation of replaceable energy dissipation connection for moment-resisting composite steel frames[J]. Journal of Structural Engineering, 2018, 144(6): 04018042.
[25] Fang C, Yam M C H, Lam A C C, et al. Cyclic performance of extended end-plate connections equipped with shape memory alloy bolts[J]. Journal of Constructional Steel Research, 2014, 94: 122-136.
[26] Guo Y, Wang M. Experimental study on mechanical behavior and resilient performance of steel frame connection with low-yield-point steel fuses[J]. Engineering Structures, 2022, 266: 114599.
[27] Wang M, Tong Y, Sun Y, et al. Structural fuse design of bolted steel frame with low yield point angle steel connection components[J]. Thin-Walled Structures, 2022, 179: 109553.
[28] Jiang Z Q, Yang X F, Zhang A L, et al. Experimental study on energy consuming devices for earthquake-resilient prefabricated cross joints[J]. Journal of Building Structures, 2020, 41(1): 15-23 (in Chinese).
[29] Jiang Z Q, Kang Y T, Liu X C, et al. Experimental study of an earthquake-resilient prefabricated opening-web steel channel beam-to-column joint with flange cover plates[J]. Engineering Structures, 2020, 221: 111054.
[30] Zhao J, Qin H, Okazaki T, et al. Seismic resilient steel moment connections with top shear tabs and bottom replaceable metallic fuse: Analytical and experimental study[J]. Engineering Structures, 2024, 306: 117789.
[31] Li G C, Qin Z W, Li X ,et al. Numerical study on the seismic performance of H-beam to embedded CFRP circular tube CFST column joint with replaceable energy dissipation angle steel[J]. Structures, 2024, 67: 106793.
[32] Ministry of Housing and Urban-Rural Development of the People's Republic of China. GB50017-2017: Standard for Design of Steel Structures, China Architecture and Building Press, Beijing, China, 2017 (in Chinese).
[33] Han L H, Yao G H, Tao Z. Performance of concrete-filled thin-walled steel tubes under pure torsion[J]. Thin-Walled Structures, 2007, 45(1): 24-36.
[34] Ministry of Housing and Urban-Rural Development of the People's Republic of China. GB/T 3098.1-2010: Mechanical properties of fasteners-Blots, screws and studs, Standards Press of China, Beijing, China, 2010 (in Chinese).
[35] American Institute of Steel Construction. Seismic Provisions for Structural Steel Buildings: ANSI/AISC 341-10[S]. Chicago: American Institute of Steel Construction, 2010.
[36] Li G C, Zhang C Y, Yu H P. Advance in high-strength concrete filled square steel tubular structure with inner CFRP circular tube[J]. Engineering Mechanics, 2012, 29(11): 57-68 (in Chinese).
[37] Wang X, Wang Y, An Q. Experimental study on seismic behavior of prefabricated beam-to-column high-strength bolted joint with external diaphragms[J]. China Civ. Eng. J, 2020, 53: 53 (in Chinese).
[38] Men J, Li T, Zhou Q, et al. Structural fuse performance and earthquake-resilient performance of beam-column joints with replaceable T-stub[J]. Journal of Constructional Steel Research, 2023, 206: 107943.
[39] Hu S W, Qi H, et al. Research on seismic performance of prelabricated beam-column joints with dog-bone style weakening beam[J]. Building Structure, 2024, 54(14): 98-105 (in Chinese).
[40] American Institute of Steel Construction. Specification for Structural Steel Buildings: AISC 360-22[S]. Farmington Hills: American Institute of Steel Construction, 2022.
[41] European Committee for Standardization. Design of steel structures: part 1.8:design of joints: EN 1993-1-8 (EC3)[S]. Brussels: European Committee for Standardization, 2005.